





Coronavirus endoribonuclease antagonizes ZBP1-mediated necroptosis and delays multiple cell death pathways

Monika Evdokimova^a, Shuchen Feng^a, Allen Caobi^{b.c}, Fernando R. Moreira^a, Dakota Jones^{d.e}, Konstantinos-Dionysios Alysandratos^{d.e}, Ena S. Tully^f, Darrell N. Kotton^{de} 🗓, David F. Boyd^g, Bridget S. Banach^h, Robert N. Kirchdoerfer^f 🗓, Mohsan Saeed^{b.c} 🗓, and Susan C. Baker^{a,1} 🗓

Affiliations are included on p. 11.

Edited by Michael Diamond, Washington University in St. Louis School of Medicine, St. Louis, MO; received September 30, 2024; accepted January 13, 2025

Identifying conserved mechanisms used by viruses to delay host innate responses can reveal potential targets for antiviral therapeutics. Here, we investigated coronavirus nonstructural protein 15 (nsp15), which encodes a highly conserved endoribonuclease (EndoU). EndoU functions as an immune antagonist by limiting the accumulation of viral replication intermediates that would otherwise be sensed by the host. Despite being a promising antiviral target, it has been difficult to develop small-molecule inhibitors that target the EndoU active site. We generated nsp15 mutants of the coronaviruses severe acute respiratory syndrome coronavirus 2 (SARS-CoV-2) and mouse hepatitis virus (MHV)-A59 and identified conserved residues within the amino-terminal domain that are required for EndoU activity. Loss of EndoU activity caused the activation of host sensors, which limited viral replication in interferon-responsive cells and attenuated disease in MHV-infected mice. Using transcriptional profiling, we found that MHV EndoU mutant viruses upregulate multiple host sensors, including Z-form nucleic acid-binding protein 1 (ZBP1). We found that nsp15 mutants induced early, robust ZBP1-mediated necroptosis. EndoU mutant viruses also induced ZBP1-independent apoptosis and pyroptosis pathways, causing early, robust cell death that limits virus replication and pathogenesis. Overall, we document the importance of the amino-terminal domain for EndoU function. We also highlight the importance of nsp15/EndoU activity for evading host sensors, delaying cell death, and promoting pathogenesis.

coronavirus | nsp15 | EndoU | ZBP1 | cell death

The interaction between a virus and its host dictates the outcome of infection. To respond to viral infection, the host must first sense the incoming pathogen. Host cells express or rapidly upregulate evolutionarily conserved pattern recognition receptors (PRRs) that function to sense viral infection by recognizing pathogen-associated molecular patterns (PAMPs), particularly double-stranded RNA (dsRNA). In turn, viruses have evolved mechanisms to evade PRRs and promote viral replication without host restriction.

Coronaviruses, including SARS-CoV-2, the causative agent of COVID-19, encode a set of viral proteins that act as immune antagonists to evade host immune sensors, delay subsequent antiviral signaling, and replicate and spread without early host restriction (1). Coronaviruses are positive-sense RNA viruses within the Nidovirales order that replicate efficiently in the respiratory and gastrointestinal tract, causing diseases that can range from mild to lethal. Following entry into cells, the coronavirus positive-sense RNA genome is translated to generate 16 nonstructural proteins, at least 4 structural proteins, and a varying number of strain-specific accessory proteins. The nonstructural proteins rearrange the host endoplasmic compartments to form double-membrane vesicles (DMVs) (2-4). These DMVs are the sites of viral replication, where the replication and transcription complex (RTC) generates positive-sense and negative-sense genomic and subgenomic RNAs. If RNA intermediates, such as dsRNA, exit the DMVs, they may be recognized by host sensors melanoma differentiation-associated protein 5 (MDA5), protein kinase R (PKR), and 2'-5' oligoadenylate synthase (OAS), leading to interferon (IFN) production, inhibition of protein translation, and degradation of cytoplasmic RNA, respectively (5-8). Activation of these sensors can also lead to the induction of cell death. Our group previously demonstrated that coronaviruses prevent early, robust activation of apoptosis during infection (5). Recently, other cell death pathways, such as pyroptosis and necroptosis, have also been found to be important during coronavirus infection (9, 10). Most recently, independent studies revealed that SARS-CoV-2 infection activates the host sensor Z-form nucleic acid-binding protein 1 (ZBP1) to drive necroptosis of infected cells, but the

Significance

Coronaviruses can expertly evade our immune system. One way they do this is by employing the viral protein nsp15. This protein contains an endoribonuclease domain (EndoU), which cleaves viral RNA that would otherwise alert the cell that an infection has begun. The catalytic site of nsp15 has been difficult to target with antivirals. We made coronavirus nsp15 mutant viruses and identified the amino-terminal domain to be equally essential for EndoU function. We found that EndoU evades several host sensors, including Z-form nucleic acid-binding protein 1 (ZBP1), to dampen a protective host interferon response and delay cell death. This allows coronaviruses to replicate to high levels and cause disease. This work identifies a potential target for the development of nsp15 antivirals.

Author contributions: M.E., R.N.K., M.S., and S.C.B. designed research; M.E., S.F., A.C., F.R.M., D.J., E.S.T., and B.S.B. performed research; K.-D.A., D.N.K., D.F.B., R.N.K., M.S., and S.C.B. contributed new reagents/analytic tools; M.E. and S.F. analyzed data; and M.E. wrote the paper.

The authors declare no competing interest.

This article is a PNAS Direct Submission.

Copyright © 2025 the Author(s), Published by PNAS. This open access article is distributed under Creative Commons Attribution-NonCommercial-NoDerivatives License 4.0 (CC BY-NC-ND).

¹To whom correspondence may be addressed. Email:

This article contains supporting information online at https://www.pnas.org/lookup/suppl/doi:10.1073/pnas. 2419620122/-/DCSupplemental.

Published March 4, 2025.

mechanism of this activation is unclear (10, 11). By preventing early innate immune responses and delaying death of infected cells, viral immune antagonists promote virus replication and disease.

One of the most highly conserved coronavirus immune antagonists is nonstructural protein 15 (nsp15). Nsp15 utilizes a histidine-histidine-lysine catalytic triad within its C-terminal domain to function as an endoribonuclease (12, 13). This endoribonuclease domain (EndoU) is conserved among all vertebrate nidoviruses, including coronaviruses and arteriviruses (14, 15). Coimmunoprecipitation and immunofluorescence experiments revealed that nsp15 is a part of the RTC and localizes to the site of viral RNA synthesis (16, 17). Because of its proximity to the site of viral RNA synthesis, EndoU activity was implicated as a potential regulator of viral replication and/or transcription. However, we and others generated viruses containing mutations within nsp15 and found that EndoU activity is not required for coronavirus replication in IFN-non-responsive cells. In this context, EndoU catalytic site mutant viruses replicate similarly to wild-type (WT) virus (5, 6, 8, 18). In contrast, the replication of coronavirus nsp15/EndoU catalytic site mutants is dramatically impaired in IFN-responsive cells, where loss of EndoU activity leads to an early, robust immune response and death of infected cells. We previously reported that infection with a catalytically inactive nsp15 mutant mouse hepatitis virus (MHV)-A59 (MHV-nsp15-H262A) leads to accumulation of an epitope recognized by the anti-dsRNA antibody K1 (5, 19). Other studies have shown that nsp15 mutants of MERS-CoV and SARS-CoV-2 also display increased dsRNA signal (7, 8). While the identity and structure of EndoU's substrate remains an active area of investigation in the field, our prior work suggests that EndoU can cleave viral polyU-containing negative-sense RNA to prevent the activation of host sensors (19). This led us to hypothesize that coronavirus negative-sense RNA may adopt a dsRNA-like conformation that acts as a PAMP and activates several host sensors, including MDA5, PKR, and OAS, to stimulate an IFN response, induce cell death, and limit viral replication.

The conservation of EndoU and its critical role during viral infection as an IFN antagonist has led to efforts in discovering small-molecule inhibitors that will bind the catalytic site of EndoU and inhibit its activity (20–23). However, there are currently no safe and effective antivirals targeting EndoU. Importantly, little is known about the role of residues outside of the EndoU active site, such as residues within the N-terminal domain (NTD) or middle domain, in regulating EndoU function. These noncatalytic sites may offer an alternative approach for inhibiting nsp15 activity.

The goals of this study were to 1) identify noncatalytic residues of nsp15 that regulate EndoU activity during virus replication and 2) to globally evaluate how loss of EndoU function results in activation of the host innate immune response and subsequent cell death. We used reverse genetics to generate SARS-CoV-2 and MHV nsp15/EndoU NTD mutant infectious viruses. We compared viral replication and innate immune antagonism of NTD mutant viruses to WT and to a nsp15 catalytic mutant and documented a critical role of the NTD in nsp15 function. To evaluate the host response to EndoU mutant virus infection, we performed transcriptional profiling and found that EndoU mutants induce the expression of multiple host PRRs, including ZBP1. We describe the role of EndoU in delaying the activation of ZBP1, and the consequences of early ZBP1 activation on the fate of coronavirus-infected macrophages. Overall, we demonstrate potential for the nsp15 NTD as a therapeutic target and reveal a role for nsp15 activity in delaying cell death through necroptosis, apoptosis, and pyroptosis during coronavirus infection.

Results

Investigating the Role of the nsp15 Amino-Terminal Domain in Coronavirus Replication. The primary amino acid sequence and structure of the nsp15 NTD is highly conserved among coronaviruses and is suggested to promote oligomerization into the active hexamer form, which is a dimer of trimers (Fig. 1 A-D) (24-26). Specifically, NTD residues L2 and E3 project from the surface of one protomer and participate in a hydrogen bonding network with residues L2 and E3 on an adjacent protomer. In this hydrogen bonding network, the backbone amino group of L2 interacts with the side chain carboxyl group of E3. These interactions occur at three distinct sites along the trimer-trimer interface (boxed in Fig. 1D). Studies with SARS-CoV have documented E3 as essential for forming the nsp15 hexamer (24, 25). This hexameric assembly has been shown to be required for in vitro nsp15 activity of multiple coronaviruses, including SARS-CoV, MERS-CoV, and SARS-CoV-2 (25–29). Here, we used the two coronaviruses MHV and SARS-CoV-2 to evaluate the role of these NTD residues in EndoU activity during coronavirus replication.

To examine the role of the nsp15 NTD in the context of viral replication, we used the circular polymerase extension reaction (CPER) method to generate NTD mutant viruses, MHV-nsp15-L2D, MHV-nsp15-E3K, and SARS-CoV-2-nsp15-E3A (SI Appendix, Fig. S1) (30–32). We report that these mutations within the MHV-A59 NTD do lead to impaired oligomerization and loss of endoribonuclease activity in vitro, consistent with a previous study on the SARS-CoV E3 residue (SI Appendix, Fig. S2) (24). The nsp15 NTD mutant viruses were recoverable and replicated to similar levels in cells deficient in the production or sensing of type 1 IFN, although the SARS-CoV-2 nsp15-E3A virus was slightly attenuated compared to the WT virus early during infection (Fig. 1 *E* and *F*). These results indicate that the nsp15 L2 and E3 residues are not essential for coronavirus replication in the absence of an IFN response. We further investigated whether NTD mutations affected the expression and localization of MHV nsp15. Using western blot studies, we found that MHV NTD mutant viruses accumulated levels of nsp15 similar to WT nsp15 during replication in BMDM cells (Fig. 2A). For coimmunoprecipitation and colocalization experiments, we introduced the nsp15-E3K mutation within the well-characterized in situ HA-tagged nsp15 virus (17). We used these two independent approaches to evaluate the association of nsp15-E3K with the RTC component nsp8. We found that MHV nsp15-E3K coimmunoprecipitated with the replicase complex protein nsp8 (Fig. 2B) and colocalized with nsp8 in the cytoplasm of MHV-infected cells (Fig. 2C), similar to WT nsp15. Overall, these results indicate that the NTD mutations did not alter the accumulation or localization of nsp15 during virus infection.

Coronavirus nsp15-NTD Mutants Are Attenuated in IFN-Responsive Cells and Cause Early, Robust Activation of the Host Innate Immune Response Compared to WT Coronavirus **Infection.** To determine whether disruption of the nsp15 NTD affects viral replication in IFN-responsive cells, we infected primary BMDMs with MHV nsp15/EndoU mutant viruses and measured the production of infectious viral particles over time. Similar to the catalytically inactive virus (MHV-nsp15-H262A), the MHV-NTD mutants were significantly attenuated in the production of infectious virus particles in BMDMs (Fig. 3A). Our lab and others have previously demonstrated that loss of catalytic EndoU activity attenuates viral replication due to the accumulation of viral dsRNA that activates host responses (5, 7, 8, 19). To assess whether disruption of the nsp15 NTD leads to increased dsRNA levels, we measured the accumulation of viral dsRNA during infection of *ifnar*^{-/-} BMDMs.

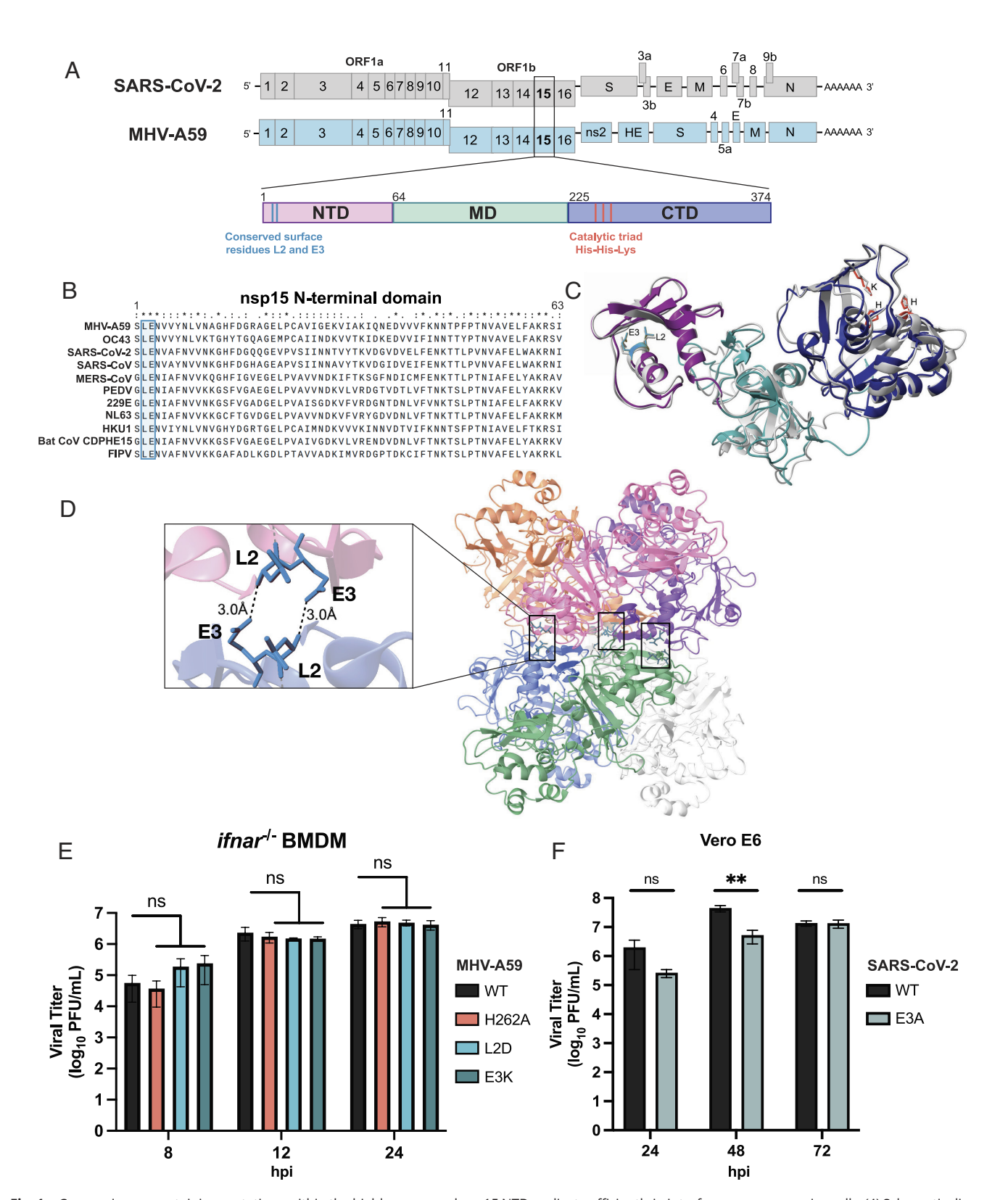
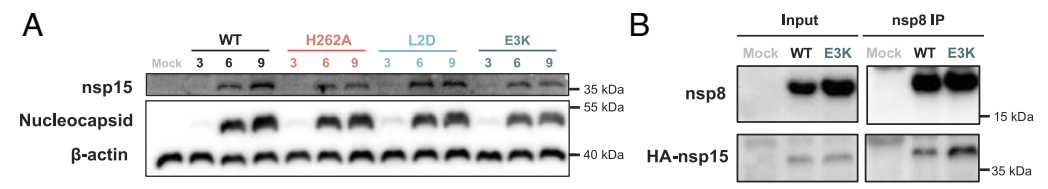


Fig. 1. Coronaviruses containing mutations within the highly conserved nsp15 NTD replicate efficiently in interferon-nonresponsive cells. (A) Schematic diagram of the genomic structure of SARS-CoV-2 and MHV-A59. Nsp15 and its three domains are highlighted. (B) Sequence alignment of the nsp15 NTD of various coronaviruses within the alpha and beta genera. The conserved NTD residues L2 and E3 are boxed. (C) A structural overlay of the monomeric nsp15 structures of SARS-CoV-2 (PDB 7RB0) in gray and MHV-A59 (PDB 2GTH) colored according to the domain. The L2 and E3 NTD residues are colored in blue and the catalytic sites residues are colored in red. (D) Model of the MHV-A59 nsp15 hexameric structure highlighting the hydrogen bonding network of L2 and E3. The L2-E3 hydrogen bonding network is located at three distinct sites along the trimer-trimer interface. Each of these sites is boxed. (E) Replication kinetics of WT MHV-A59, MHV-nsp15-H262A, -L2D, and -E3K mutant viruses in ifnar-1- BMDM cells infected at an MOI of 0.2. Data were analyzed with a two-way ANOVA (ns P > 0.05). Results are representative of three independent replicates and represented as mean ± SD. (F) Replication kinetics of WT SARS-CoV-2 and SARS-CoV-2-nsp15-E3A mutant in Vero E6 cells infected at an MOI of 0.1. Data are representative of three independent experiments and were analyzed using an unpaired t test (ns P > 0.05; **P < 0.01).



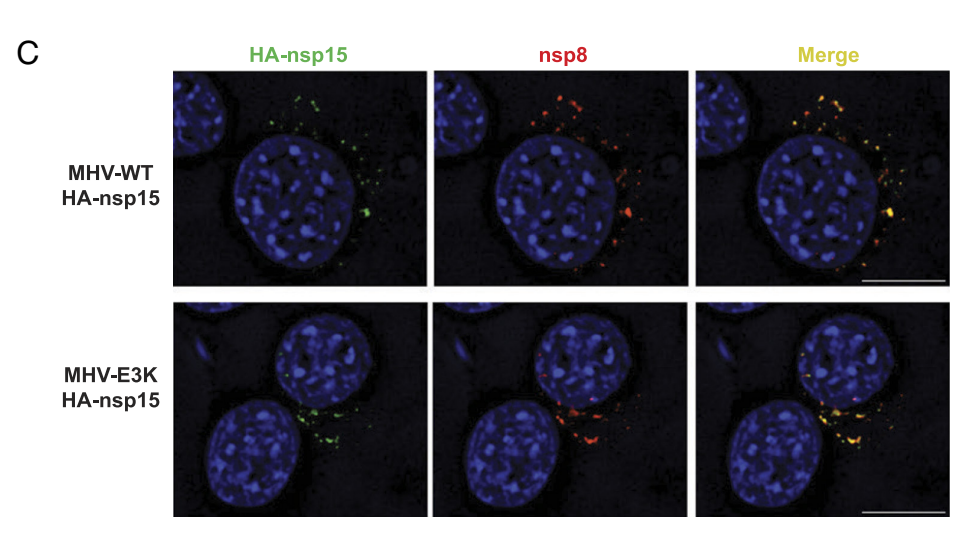


Fig. 2. Coronavirus nsp15/EndoU mutant proteins are expressed at levels similar to WT protein and colocalize with the viral replicase complex. (A) Lysates from BMDM cells infected at an MOI of 1.0 for the indicated time were probed by western blot for detection of nsp15, nucleocapsid, and B-actin. Results are representative of two independent experiments. (B) Western blot detection of nsp15 coimmunoprecipitated with replicase component nsp8. Lysates were prepared from BHK-R cells infected with MHV-WT-HA or -E3K-HA viruses at an MOI of 0.01. The input cell lysates and subsequent immunoprecipitated lysates were blotted with anti-HA or anti-nsp8. Results are representative of three independent experiments. (C) Colocalization of WT nsp15 and E3K nsp15 with replicase component nsp8. 17Cl-1 cells were infected at an MOI of 1.0 for 6 h with either MHV-WT-HA or -E3K-HA. Cells were fixed, permeabilized, and stained with anti-HA and anti-nsp8. Images are representative of at least 50 cells. Scale bars set to 5 µm are shown.

In this cell type, EndoU mutant viruses are not attenuated and replicate similarly to WT virus (Fig. 1*E*). Interestingly, we observed a statistically significant increase in the accumulation of viral dsRNA during infection with the NTD mutant viruses as compared to WT (Fig. 3B). This suggests that nsp15 NTD mutant viruses exhibit impaired EndoU activity. To investigate whether the coronavirus nsp15-NTD mutants activate type I IFN responses, we measured the levels of IFN in two different types of IFN-responsive virusinfected cells. We detected significantly higher levels of IFN α 11 mRNA in primary BMDMs infected with MHV-NTD mutants compared to MHV-WT (Fig. 3C). This was also true for MHVnsp15-H262A, which also induced higher levels of IFNα11 expression. A similar phenotype was observed in mouse hepatocyte cells, AML12 cells, which also express and respond to interferon (Fig. 3D). To examine the levels of interferon protein production, we measured the amount of secreted IFN α and observed robust IFN α secretion from BMDMs infected with nsp15 mutant viruses (Fig. 3E). We then evaluated the activation of the host antiviral sensor OAS, which senses dsRNA and activates RNase L, leading to degradation of cytoplasmic RNA. Again, the MHV-NTD mutant viruses led to earlier and significantly more robust degradation of host RNA as compared to MHV-WT (Fig. 3F). We extended our evaluation of the nsp15 NTD to SARS-CoV-2 by infecting human induced pluripotent stem cell (iPSC)-derived alveolar epithelial type II cells (iAT2s) with the E3A NTD mutant SARS-CoV-2 virus and measured viral titers over time. We also included H234A SARS-CoV-2 virus as a catalytically inactive control. Despite similar viral titers at the start, E3A and H234A titers dramatically decreased over time compared to WT virus, indicating decreased production of infectious progeny virus (Fig. 4A). By 4 days postinfection (dpi), the SARS-CoV-2 E3A mutant virus exhibited 200-fold lower titers compared to WT virus. We also used iAT2s to assess the induction of interferon-stimulated genes (ISGs), as these cells have an intact innate immune system and respond to viral infections by upregulating ISGs (33). We found that the SARS-CoV-2 E3A virus stimulated an earlier and more robust innate immune response compared to WT virus in these cells (Fig. 4 B–D). The earlier and more robust induction in ISG expression by E3A was similar to H234A infection, again demonstrating the importance of the nsp15

NTD. These results suggest that mutations within the NTD of nsp15 impair EndoU activity, which is critical for delaying host innate immune responses to virus infection.

Global Transcriptional Profiling Reveals Induction of Multiple Host Pattern Recognition Receptors During MHV-nsp15/EndoU **Mutant Virus Infection.** To further investigate how nsp15 function modulates the host response to infection, we performed RNA sequencing on primary BMDMs infected with WT MHV-A59 or the nsp15 mutant viruses. We used nonmetric multidimensional scaling (NMDS) analysis to visualize global changes in the host transcriptome based on the differentially expressed genes (DEGs) detected during each infection (Fig. 5A). We found that at 3 hours postinfection (hpi), all the infection conditions grouped together with similar transcriptomic profiles. As early as 6 hpi, the different infection conditions began to spatially spread apart, indicating differentiation of global transcriptomes in the WT and nsp15/EndoU mutant virus-infected cells. By 9 and 12 hpi, the WT infection condition grouped separately from the nsp15 mutant viruses, illustrating the dramatic differences in the host response to infection with and without EndoU activity. Focusing on the top 1% of abundant DEGs (Fig. 5*B*), we noted that IFNs, ISGs, and dsRNA sensors were upregulated earlier in response to infection with nsp15 mutants as compared to WT virus (Fig. 5 C-E). In this analysis, we noted that the host sensor ZBP1 was upregulated during H262A, L2D, and E3K infection compared to WT. Unlike the other dsRNA sensors, ZBP1 has not been well characterized in the context of nsp15 mutant coronavirus infection and has been documented to bind Z-form RNA that is folded in the more unusual and rare left-handed conformation (34, 35). Previous studies reported that ZBP1 senses viral RNA to activate necroptosis of infected cells and that viral antagonism of ZBP1 is important in the pathogenesis of other viral infections (34–37). In support of this, transcriptional pathway analysis revealed that the necroptosis pathway was one of the top 15 KEGG pathways upregulated during all three nsp15 mutant virus infections (SI Appendix, Fig. S4). We calculated the gene ratio of this pathway by dividing the number of necroptosis pathway DEGs by the total number of genes within the necroptosis pathway. Compared to

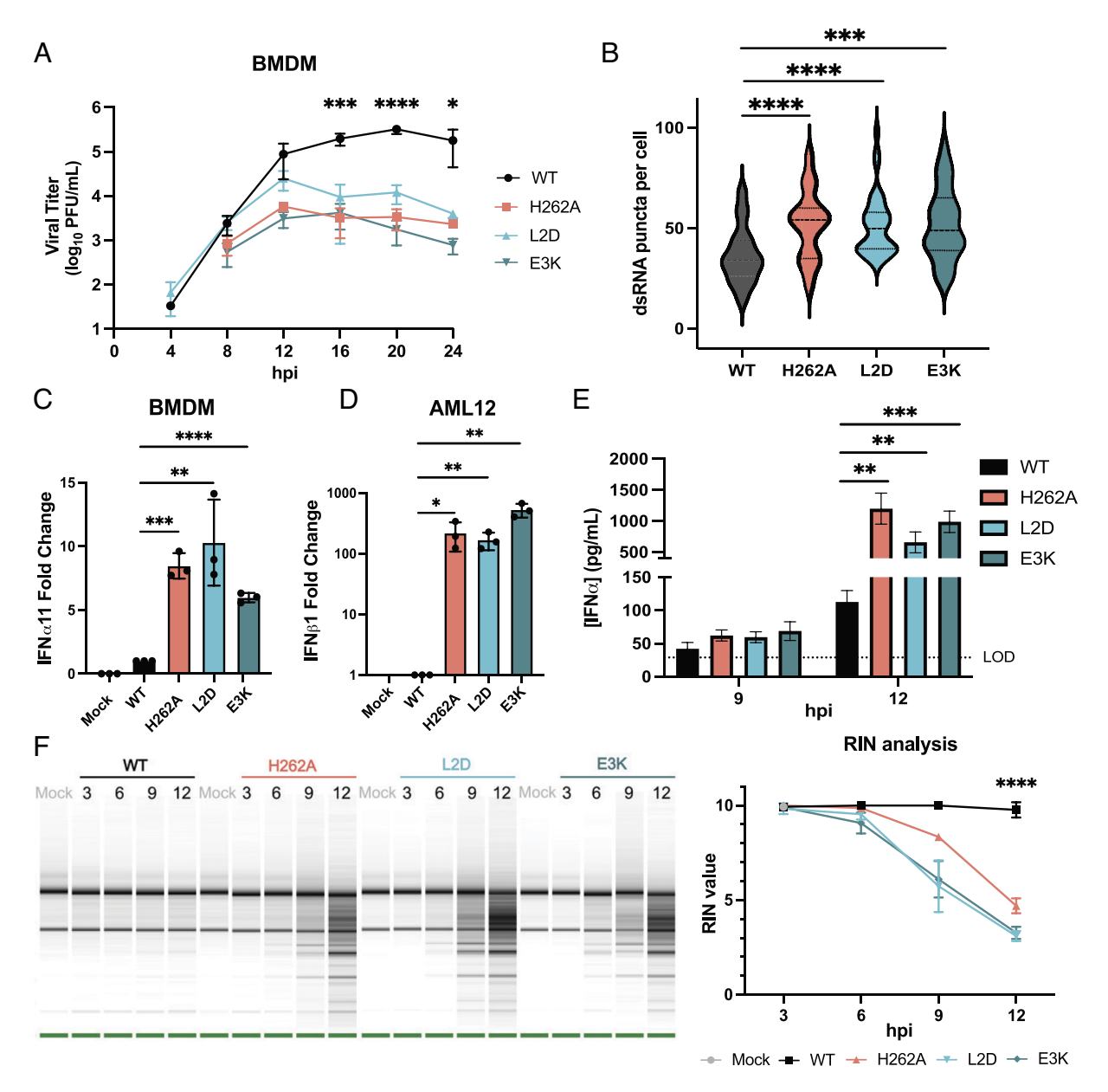


Fig. 3. MHV NTD mutants are attenuated in interferon-responsive cells and activate multiple host immune sensors. (A) WT BMDMs were infected at an MOI of 0.2 with either WT, H262A, L2D, or E3K MHV viruses. Viral titers were measured by plaque assays at indicated timepoints. Data are representative of three independent replicates and represented as mean \pm SD. Values were analyzed using a one-way ANOVA at the indicated timepoint (*P < 0.05; ***P \leq 0.0002; *****P < 0.0001). (B) ifnar^{-/-} BMDMs were infected at an MOI of 0.1 with the indicated virus. Cells were fixed at 5 hpi, permeabilized, and stained with anti-dsRNA. For each infection condition, the number of dsRNA puncta per cell was quantified for 35 cells. Each violin plot depicts the median (Middle dashed line) and two quartile lines above and below the median. Values were analyzed using an unpaired t test (***P < 0.001; ****P < 0.0001). Data are representative of two to three independent experiments. Representative immunofluorescence images for each infection condition can be found in SI Appendix, Fig. S3. (C and D) Evaluating activation of the type I interferon response in BMDM (C) and AML12 (D) cells. BMDMs were infected at an MOI of 0.1 for 12 h. AML12s were infected at an MOI of 1.0 for 24 h. At the indicated time, RNA was isolated for RT-qPCR analysis with primers to amplify IFNα11 or IFNβ1 and normalized to 18S rRNA. Results are representative of three independent replicates. Data were analyzed using an unpaired t test (*P < 0.05; **P < 0.01; ***P < 0.001; ****P < 0.0001). (E) WT BMDMs were infected at an MOI of 0.1 with the indicated virus. At 9 and 12 hpi, supernatants were collected and used to evaluate the levels of mouse IFNα by ELISA. Data are representative of three independent replicates and represented as mean ± SD. Values were analyzed using an unpaired t test at 12 hpi (**P < 0.01; ***P < 0.001). (A) Evaluating activation of OAS/RNase L. BMDMs were infected at a MOI of 1.0 with WT, H262A, L2D, or E3K MHV viruses. At the indicated time, RNA was isolated and run on a bioanalyzer. RNA Integrity Numbers (RIN) were plotted and showed statistically significant (****P < 0.0001) differences in RNA integrity between the WT MHV-A59 and nsp15-mutant virus infections with a one-way ANOVA at 12 hpi.

WT infection, the necroptosis pathway gene ratio was higher for all three nsp15 mutant viruses at all three timepoints (Fig. 5F). Therefore, we hypothesized that nsp15/EndoU activity may prevent the activation of ZBP1 and other host sensors that would normally activate cell death pathways and limit virus replication.

Coronavirus nsp15/EndoU Mutants Activate ZBP1-Mediated Necroptosis and Promote Multiple Programmed Cell Death Pathways. To evaluate whether loss of EndoU activity promotes early cell death, we performed a viability assay in primary BMDMs. We observed a rapid and robust induction of cell death during infection with MHV-nsp15 mutant viruses (Fig. 6A). Whereas other cell death pathways, such as apoptosis and pyroptosis, depend on caspases, necroptosis is a caspase-independent cell death mechanism. To determine whether MHV-nsp15/EndoU mutant viruses activated necroptotic cell death, we treated BMDMs with the pan-caspase inhibitor Z-VAD-FMK (zVAD) and evaluated the levels of phosphorylated RIPK1 (pRIPK1), phosphorylated

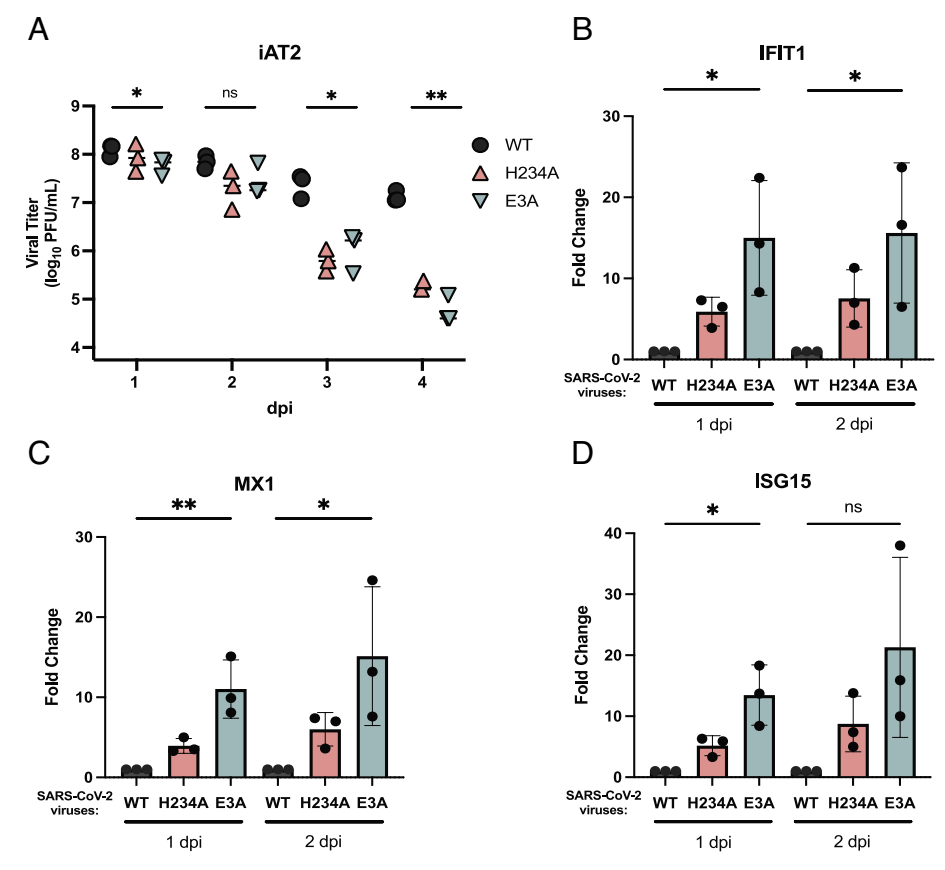


Fig. 4. A SARS-CoV-2 nsp15 NTD mutant virus is attenuated in iAT2 cells and induces early, robust induction of ISG expression. (A) iAT2s were infected at an MOI of 0.3 with WT SARS-CoV-2, the H234A catalytically inactive mutant virus, or the E3A NTD mutant virus. Supernatants were harvested for plaque assay on the indicated days. On 4 dpi, one of the H234A replicates had undetectable viral titers and is not depicted on the graph. Data are representative of three independent experiments. Values were analyzed with an unpaired t test (ns > 0.05, *P < 0.05; **P < 0.01). (B-D) Evaluating expression of interferon-stimulated genes induced after SARS-CoV-2 infection, iAT2 cells were infected at an MOI of 0.3 with WT SARS-CoV-2, H234A, or the E3A NTD mutant virus. Cells were harvested on 1 or 2 dpi. RNA was isolated and used for RT-qPCR analysis with primers specific to human IFIT1, MX1, or ISG15 and normalized to 18S rRNA. Results are representative of three independent experiments and were analyzed with an unpaired t test (ns P > 0.05; *P < 0.05; **P < 0.01). All data are represented as mean ± SD.

RIPK3 (pRIPK3), and phosphorylated MLKL (pMLKL), all markers of necroptosis, using western blotting (Fig. 6B). We found that all three nsp15 mutant viruses induced higher levels of pRIPK1, pRIPK3, and pMLKL, as compared to BMDMs infected with WT MHV-A59, which had no detectable levels of these markers. To determine whether this induction of necroptosis depended on ZBP1, we performed the same experiment in $\hat{Zbp1}^{-1}$ BMDMs. ZBP1 can induce necroptosis by directly promoting RIPK3 phosphorylation and also by functioning as a scaffold that recruits and activates RIPK1, which can then also phosphorylate RIPK3 (38). In support of our hypothesis, the induction of pRIPK1, pRIPK3, and pMLKL during nsp15 mutant infection was decreased in Zbp1^{-f-} BMDMs, compared to WT BMDMs (Fig. 6B). We note that even in the absence of ZBP1, nsp15 mutant viruses did induce increased levels of pRIPK1, pRIPK3, and pMLKL compared to WT infection, suggesting that loss of EndoU activity can also drive ZBP1-independent necroptosis in BMDMs. These ZBP1-independent necroptosis pathways have been described previously in BMDMs and include the RIPK1dependent TNFα signaling pathway (39). Since we observed high levels of pRIPK1 during nsp15 mutant infection of Zbp1^{-/-} BMDMs, we hypothesized that the ZBP1-independent necroptosis driven by nsp15 mutant viruses was RIPK1-dependent. To test this, we treated Zbp1^{-/-} BMDMs with zVAD and GSK'963, a RIPK1 inhibitor. We found that inhibition of RIPK1 reduced the levels of pRIPK3 and pMLKL to undetectable levels (SI Appendix, Fig. S5). These data suggest that the rapid and robust accumulation of viral PAMPs generated during MHV-nsp15-mutant infection can activate ZBP1, promoting the necroptotic cell death pathway. Even in the absence of ZBP1, nsp15 mutant viruses induce RIPK1-dependent necroptosis. We also evaluated whether loss of EndoU activity could activate other cell death pathways, such as pyroptosis and apoptosis. We probed for the initiator caspase-8 and executioner caspase-3, both markers of apoptosis. We found

that EndoU mutant viruses induced earlier and higher levels of cleaved, active caspase-3 and -8 (Fig. 6C). We also probed for cleaved gasdermin-D (GSDMD) protein, indicative of pyroptosis, and again noted that only EndoU mutant virus infection led to cleavage of GSDMD (Fig. 6C). We observed several GSDMD cleavage products, including the p30 product that is known to form pores in the membrane and cause pyroptosis (40, 41). The additional cleavage products have been previously characterized as GSDMD cleavage by apoptotic caspase-3 and are thought to serve as a negative feedback mechanism to prevent excessive cell lysis (42-44). We note that these pathways of apoptotic caspase activation and pyroptotic GSDMD cleavage were also observed upon EndoU mutant infection in Zbp1^{-/-} BMDMs, supporting the idea that EndoU antagonizes a multitude of host sensors that regulate cell death (SI Appendix, Fig. S6). These other host sensors likely include PKR and OAS. EndoU mutant viruses have been previously reported to activate PKR (5, 7, 8), which induces apoptosis (45, 46). Additionally, the robust degradation of host RNA that is induced by EndoU mutant infection (Fig. 3F) through the OAS/RNaseL pathway can also induce apoptosis (47). Recent studies have also documented that the inflammasome senses coronavirus infection to activate pyroptosis (48, 49). Overall, the results shown here reveal that coronavirus nsp15/ EndoU activity is required to prevent early, robust activation of several host PRRs, including ZBP1, that lead to the induction of multiple, independent cell death pathways (Fig. 6D).

Coronavirus nsp15-NTD Mutant Viruses Are Highly Attenuated In Vivo. To investigate whether the early, robust activation of the innate immune response and subsequent cell death limits the generation of progeny virus and attenuates viral infection in vivo, we intraperitoneally inoculated mice with 6×10^4 PFU of WT MHV or nsp15 mutant viruses and monitored disease progression. Mice infected with WT MHV-A59 began losing weight as early as

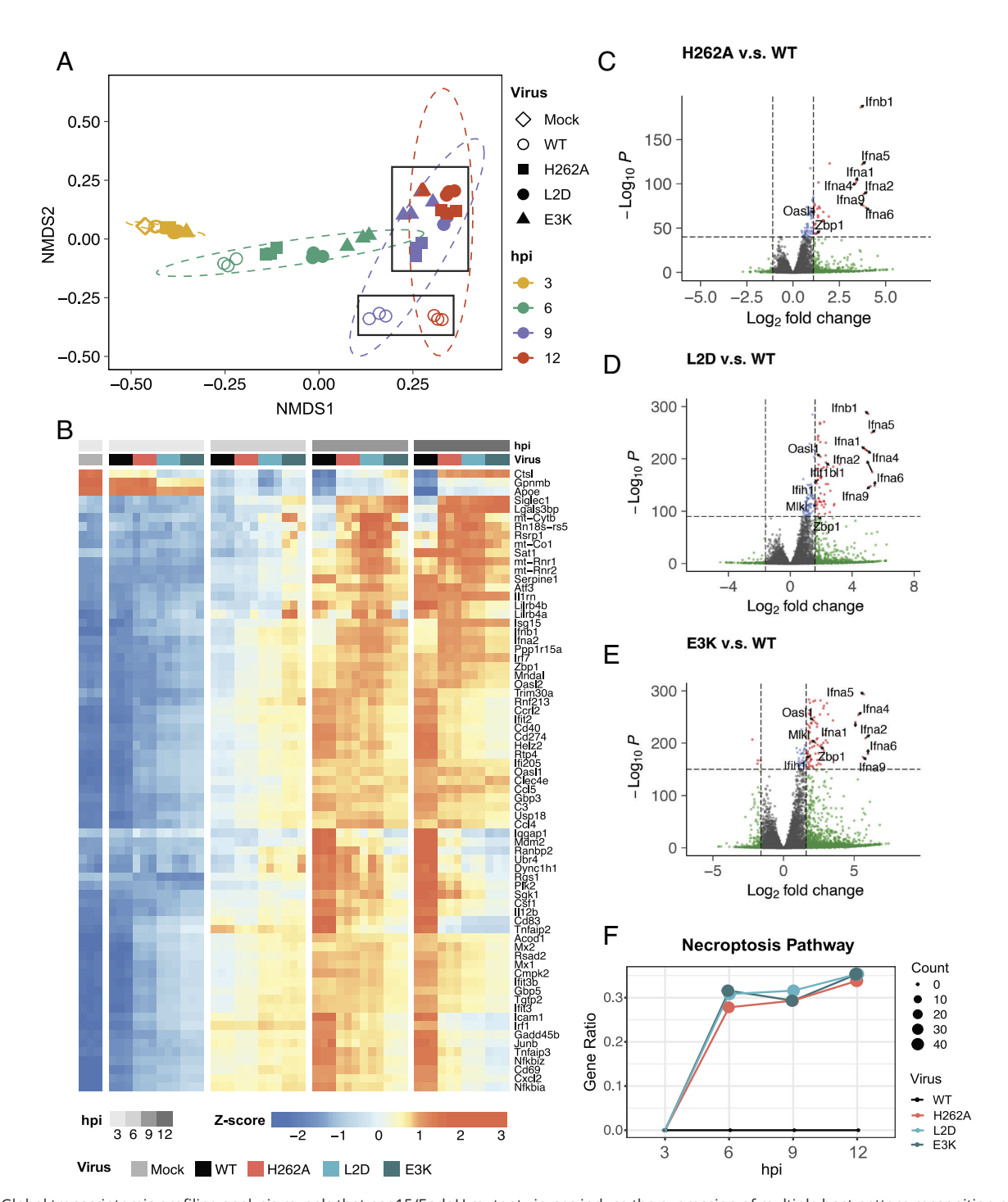
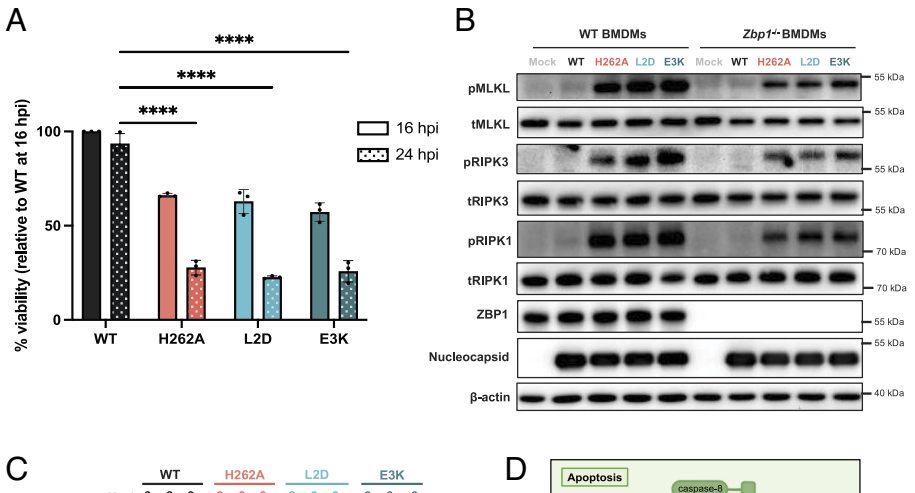


Fig. 5. Global transcriptomic profiling analysis reveals that nsp15/EndoU mutant viruses induce the expression of multiple host pattern recognition receptors and interferon-stimulated genes during replication. (A) NMDS analysis of whole transcriptome sequencing of BMDMs infected at an MOI of 1.0 with either mock, WT MHV-A59, MHV-nsp15-H262A, -L2D, or -E3K at 3, 6, 9, and 12 hpi. Ellipses represent 95% confidence levels for each group. Black boxes emphasize grouping of the host response to WT MHV away from the host response to infection with the nsp15 mutant viruses. (B) Heat map depicting the top 1% of abundant DEGs. The hpi is shown in gradient gray colors, and MHV viruses are annotated in different colors at the Top. The heatmap color intensity is associated with the normalized abundance of each DEG. The relative intensities (Z-score) are scaled from blue (low intensity) to orange (high intensity). (C-E) Volcano plots showing DEG profiles of H262A (C), L2D (D), and E3K (E) -infected cells compared to WT-infected cells at 6 hpi. Genes above the selected significance (-log₁₀ transformed P-value) and fold changes (log₂ transformed) are indicated in red dots; IFN and dsRNA sensor genes are labeled. (F) Gene ratios of the predicted necroptosis pathway in WT MHV and nsp15-mutant-infected cells. Data are representative of three independent experiments at each timepoint.

1 dpi and went on to lose an average of 13% of their weight by 5 dpi (Fig. 7A). In contrast, mice infected with NTD mutant viruses maintained their weight throughout the course of the experiment. Mice infected with WT virus had high viral titers in both the liver and spleen on 3 dpi and these titers remained high on 5 dpi, while mice infected with the NTD mutant viruses had no detectable viral titers in either spleen or liver on day 3 or day 5 postinfection (Fig. 7 B and C). Histological analysis of infected livers showed

a high number of necroinflammatory foci in the livers of mice infected with WT virus, whereas only 0 to 1 foci per 10× field were detected in the MHV-nsp15 mutant-infected mice (Fig. 7 D and E). The reduced pathogenesis of nsp15 mutant viruses can be attributed to an inability to evade the host innate immune response, as nsp15 mutant viruses caused morbidity and mortality in *ifnar*^{-/-} mice that are not IFN-responsive (*SI Appendix*, Fig. S7). These results demonstrate that nsp15 plays a significant role in



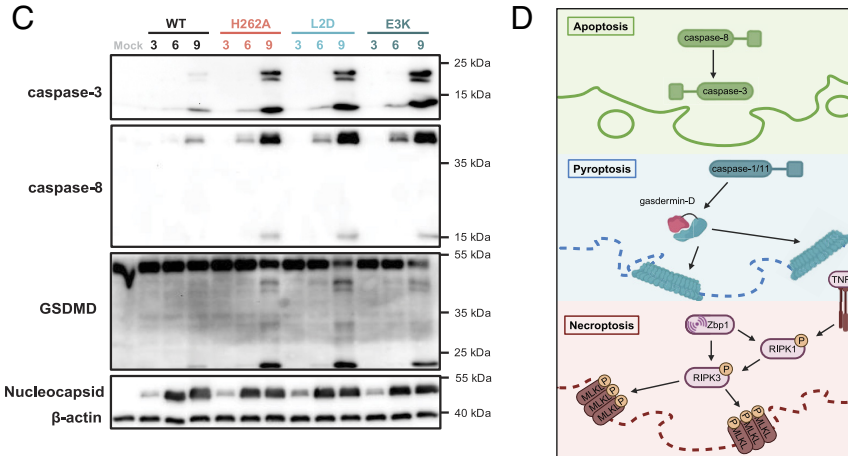


Fig. 6. Coronavirus nsp15/EndoU mutants activate ZBP1-mediated necroptosis and promote multiple programmed cell death pathways. (A) Viability assay after coronavirus infection. BMDMs were infected at an MOI of 0.1 with WT MHV-A59, MHV-nsp15-H262A, -L2D, or -E3K. Cell viability was measured by CellTiter-Glo assay at 16 or 24 hpi. Results are set relative to the cell viability of WT-infected cells at 16 hpi. Data are representative of three independent experiments and represented as the mean ± SD. Statistical analysis was performed using a one-way ANOVA at 24 hpi (****P < 0.0001). (B) Western blot detection of markers of necroptosis. WT BMDMs or Zbp1^{-/-} BMDMs infected at an MOI of 1.0 with the indicated viruses were treated with 20 µM Z-VAD-FMK at 5 hpi and harvested at 9 hpi to evaluate levels of pMLKL, tMLKL, pRIPK3, tRIPK3, pRIPK1, tRIPK1, ZBP1, nucleocapsid, and β-actin. Data are representative of three independent experiments. (C) Evaluation of coronavirus-induced activation of apoptotic and pyroptotic cell death markers. Lysates were harvested at the indicated times to evaluate cleaved caspase-3, cleaved caspase-8, GSDMD, nucleocapsid, and β-actin expression by western blot. Results are representative of three independent experiments. (D) Schematic diagram of the apoptosis, pyroptosis, and necroptosis programmed cell death pathways.

facilitating higher levels of virus replication and pathogenesis in vivo. Overall, our findings indicate that disruption of the nsp15 NTD impairs nsp15 activity in vitro, during viral replication in primary cells, and in vivo.

Discussion

Here, we report that the NTD and catalytic site of nsp15 are equally essential for its ability to delay the activation of host innate immune responses. We found that nsp15 functions to prevent viral RNA from activating ZBP1-mediated necroptosis. During MHV-A59 infection of BMDM cells, nsp15 activity not only delayed the induction of necroptosis but also delayed other cell death mechanisms, including apoptosis and pyroptosis. These data highlight the key role that EndoU activity plays in reducing the level of viral PAMPs that would otherwise activate host sensors. EndoU activity prevents the early innate immune response and delays programmed cell death in response to infection. This makes EndoU activity a promising target for the development of antivirals.

Despite research on the nsp15 catalytic site, developing antivirals that bind to the shallow catalytic pocket has proven challenging. Our study shows that the NTD of nsp15 is equally essential for its activity and may represent a more feasible target for antiviral drug development. We also highlight the importance of the nsp15 NTD in both MHV-A59 and SARS-CoV-2, suggesting that targeting the NTD could offer broad-spectrum protection against multiple coronaviruses.

The role of EndoU in antagonizing innate immune responses is highly conserved and has been reported for SARS-CoV-2, MERS-CoV, MHV-A59, and other coronaviruses (5–8, 50). These studies focused on inactivation of the catalytic site, which led to

elevated levels of ISGs in primary IFN-responsive cells and nasal epithelial cells. Here, we found that disruption of either the NTD or catalytic site of nsp15 impairs nsp15 function and promotes the activation of host dsRNA sensors. Our group and several others have previously demonstrated that during viral replication, nsp15 evades the activation of host dsRNA sensors by limiting the accumulation of dsRNA PAMPs (5–8, 19). If left uncleaved by nsp15, these dsRNA PAMPs are capable of activating A-form dsRNA sensors (MDA5, PKR, OAS) to promote several innate immune signaling pathways. Here, we extended this previous work and evaluated pathways activated by both catalytic and noncatalytic EndoU mutant viruses, revealing the transcriptional activation of genes involved in the necroptotic cell death pathway, particularly ZBP1.

ZBP1 is a host sensor that contains two Z α domains, which are also present in the human ADAR1 protein and have been well documented to bind both DNA and RNA that adopt the left-handed Z-form nucleic acid (Z-NA) structure (51, 52). We unexpectedly found that during coronavirus infection, EndoU activity functions to delay the induction of necroptosis through ZBP1. We hypothesize that the negative-sense substrate of EndoU could adopt conformations that activate A-form dsRNA sensors, as well as the Z-form sensor ZBP1. Indeed, two groups recently reported that SARS-CoV-2 infection leads to the generation of Z-RNA, but the identity of this Z-RNA was not characterized (10, 11). This Z-RNA signal was detected late in infection and may be dampened early in infection due to EndoU activity. Future studies will be aimed at characterizing the identity and structure of the viral PAMP that binds to ZBP1, and how its conformation might be changed upon cleavage by nsp15.

The activation of ZBP1 has important consequences for the fate of the cell. Following binding to its PAMP, ZBP1 recruits the RIPK3

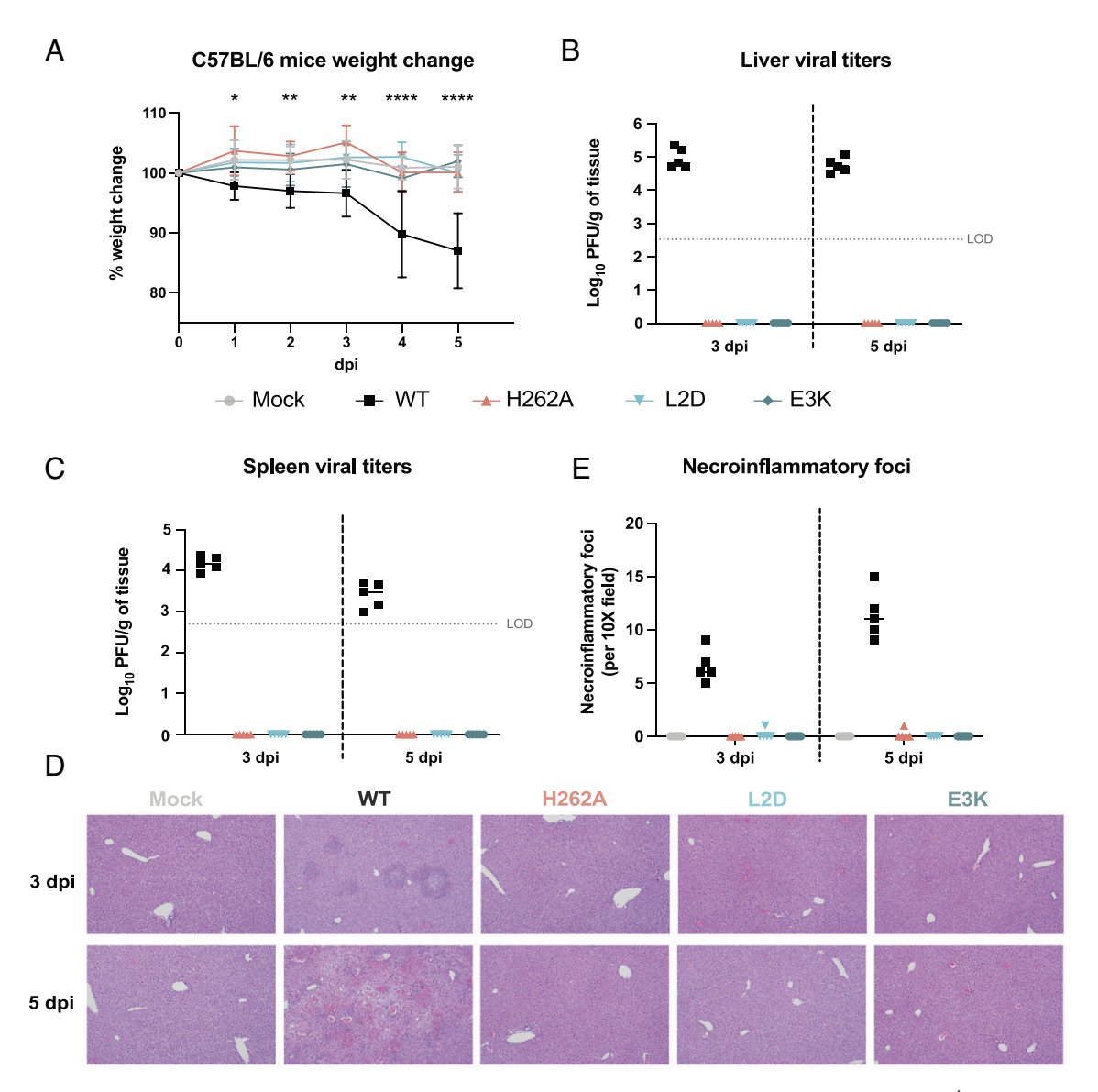


Fig. 7. Coronavirus NTD mutant viruses are highly attenuated in vivo. (A) C57BL/6 male mice (10 per group) were infected with 6 × 10⁴ PFU of either WT MHV-A59, nsp15-H262A, -L2D, or -E3K virus. Mice were weighed daily. Five mice per group were harvested on day 3, and the remaining mice were harvested on day 5. Weight loss of WT-infected mice compared to mock was significantly different at all time points, with days 4 and 5 at P < 0.0001 using a two-way ANOVA. Data are represented as mean ± SD. (B and C) Evaluating viral titers in the liver (B) and spleen (C), as assessed by plaque assay. (D) Representative images of H&E staining of infected liver tissue. Images are representative of five mice, with images taken at 10× magnification. (E) Quantitation of necroinflammatory foci per 10× field of each condition (average of 10 fields per section).

kinase to auto-phosphorylate and subsequently phosphorylate the pseudokinase MLKL. Phosphorylated MLKL oligomerizes and inserts itself into the plasma membrane, compromising membrane integrity and inducing necroptotic cell death. We found that early during MHV-A59 infection, loss of nsp15 activity led to higher levels of phosphorylated MLKL compared to WT virus. This highlights the important role of nsp15 in preventing early activation of ZBP1-mediated necroptosis. We also found that the residual necroptotic markers activated in the absence of ZBP1 were mainly driven by RIPK1, which is activated by pathways such as TNFα signaling (39).

Recent studies have highlighted the role of necroptosis in SARS-CoV-2 pathogenesis. MLKL phosphorylation has been observed during SARS-CoV-2 infection in a variety of cell types, including lung epithelial cells, neutrophils, adipocytes, pancreatic islets, and platelets (53–56). Using human lung epithelial Calu-3 cells, Li et al. recently showed that Z-NA is generated during SARS-CoV-2 infection, leading to ZBP1 activation and subsequent induction of necroptosis (11). The authors further confirmed their

findings in vivo and showed that genetic ablation of ZBP1 reduced SARS-CoV-2 pathogenicity in human ACE2-expressing mice. Our initial investigations in iAT2 cells revealed limited expression of ZBP1 at both the RNA and protein levels, reducing the utility of this cell system for necroptosis studies. We are currently developing improved model systems to investigate the role of nsp15 endonuclease activity in regulating necroptosis and inflammation during SARS-CoV-2 infection. The results of this work will be detailed in a separate manuscript, which is currently in preparation.

It is now clear that many pathogenic DNA and RNA viruses have evolved independent mechanisms to target ZBP1 and prevent early cell death. Poxviruses encode the E3 protein that has a Z-NA binding domain that competes with ZBP1 for binding to viral RNA intermediates, thus preventing necroptosis (37). Herpes simplex virus type 1 (HSV-1) encodes ICP6 that binds to RIPK3 and prevents phosphorylation of MLKL, thus blocking activation of necroptosis (57). Due to its inflammatory nature, the induction of necroptosis can have dramatic consequences for the outcome of infection. For example, recent studies using

influenza A virus (IAV) found that viral replication induces the generation of defective viral genomes that induce ZBP1-mediated necroptosis and drive IAV disease severity (36). Interestingly, Gautam et al. developed a RIPK3 inhibitor that specifically prevented necroptosis, but not apoptosis, during IAV infection (58). While this strategy did not affect viral titers in the lungs of infected mice, it did lead to reduced lung injury and enhanced survival. This work illustrates the role of necroptosis in driving disease severity after infection with IAV (58). While uncontrolled viral-induced necroptosis can exacerbate disease in some cases, early and controlled necroptosis is a highly effective antiviral mechanism that can lead to clearance of infected cells and activation of innate and adaptive immunity (59). Future studies evaluating inhibition of necroptosis during coronavirus infection will be important for identifying whether similar or distinct mechanisms drive beneficial and pathogenic responses to IAV and coronavirus infections.

As the importance of several cell death pathways is becoming more appreciated, the potential for crosstalk between these pathways has become an active area of research in the cell death field. Whether multiple cell death pathways can be engaged in a single cell remains a controversial question. The activation of pyroptosis, apoptosis, and necroptosis, known as PANoptosis, has been described to occur during several viral infections, including MHV and SARS-CoV-2 (9). In contrast, another group used single-cell imaging to emphasize the occurrence of necroptosis in SARS-CoV-2-infected cells and apoptosis in bystander cells (10). It is likely that the ability of multiple cell death pathways to be engaged simultaneously depends on cell type, particularly on which sensors and pathways are active in a given cell. We report here that EndoU mutant viruses induce early and robust activation of pyroptosis, apoptosis, and necroptosis in BMDM cells, which are known to express a multitude of host sensors. The early induction of innate immunity and cell death prevents viral propagation, leading to attenuation of viral replication in cell culture and in vivo. This protective effect is likely due to the timing of the immune response and of cell death. Studies with SARS-CoV previously demonstrated the importance of early versus late interferon treatment during infection, with early treatment causing viral clearance and mild disease and late treatment promoting inflammation and severe disease (60). This was further corroborated by Karki et al., who recently studied the effect of interferon treatment on the activation of cell death pathways after coronavirus infection (9). The authors found that interferon treatment following coronavirus infection caused more robust activation of PANoptosis in BMDM cells, leading to inflammation and lethality in mice. The importance of the timing of the host response in dictating the course of infection is a key consideration for interferon-based therapies.

In summary, this study documents the role of the coronavirus endoribonuclease in limiting the accumulation of viral PAMPs that activate host PRRs. EndoU activity is controlled by conserved amino acids in the catalytic site as well as in the amino-terminal domain, which provides independent targets for antiviral drug development. We report the key role of EndoU activity in dampening the host innate immune response and delaying the induction of cell death. We show that inactivating EndoU in the context of infectious virus attenuates viral replication and pathogenesis in IFN-responsive systems. Further studies are needed to determine whether viral negative-sense RNA or other replication intermediates form Z-RNA structures that are recognized by ZBP1 and whether this coronavirus Z-RNA contains multiple ZBP1 binding sites. Understanding the mechanisms coronaviruses use to prevent host recognition of viral RNA provides new opportunities for therapeutic interventions.

Materials and Methods

Cells. Murine fibroblast 17Cl-1 cells, baby hamster kidney cells expressing the murine coronavirus receptor (BHK-R cells), mouse hepatocyte AML12 cells (ATCC), African green monkey kidney Vero E6 cells (ATCC), Caco-2/AT cells (ATCC), and primary differentiated bone marrow-derived macrophages (BMDM cells) were all maintained in Dulbecco's Modified Eagle's Medium. L929 cells were maintained in Minimum Essential Medium. All experiments with human pluripotent stem cell lines were performed using a deidentified sample and with the approval of the Institutional Review Board of Boston University (protocol H33122). Human iPSC-derived alveolar epithelial type II cells (iAT2s) were derived from the SPC2 iPSC line carrying a SFTPC^{tdTomato} reporter (SPC2-ST-B2 clone) and cultured as detailed in *SI Appendix* (61).

Mouse Lines. C57BL/6J mice were obtained from The Jackson Laboratory. ifnar^{-/-} mice were a gift from Deborah Lenschow at Washington University in St. Louis, MO. Zbp1^{-/-} mice (David Boyd at University of California in Santa Cruz, CA) have been described previously and were used to isolate bone marrow cells (62).

MHV. The MHV strain A59 genome (GenBank AY910861.1) was previously cloned into seven plasmids that were expanded, isolated, and sequenced. These plasmids were adapted to the CPER approach, which has been described for use with SARS-CoV-2 (30-32). Additional details are provided in *SI Appendix*.

SARS-CoV-2. The SARS-CoV-2 Washington isolate containing the spike D614G substitution, with no further mutation (WT) or with the H234A or E3A mutation within nsp15, was produced in and titrated on Caco-2/AT cells as detailed in SI Appendix.

Isolation and Differentiation of Murine Primary Macrophages. Femurs were obtained from C57BL/6J, ifnar^{-/-}, or $Zbp1^{-/-}$ mice. From femurs, bone marrow cells were collected and differentiated into BMDM cells, as previously described (5). To generate L929 supernatant for BMDM media, 3.75×10^5 L929 cells were plated in T175 tissue culture flasks with 75 mL of L929 media. After 6 d of incubation at 37 °C in a 5% CO₂ incubator, the supernatant was harvested, filtered, aliquoted, and stored at -20 °C for subsequent use.

Antibodies and Other Reagents. Rabbit anti-serum against nsp8 and nsp15 were generated by our lab and have been described previously (2, 16). Mouse anti-nucleocapsid antibody (J.3.3) was generously provided by John Fleming at University of Wisconsin-Madison. The following primary antibodies were used at the indicated dilutions unless otherwise specified: mouse β-actin 1:5,000 (GenScript A00702), mouse anti-HA 1:500 (BioLegend 901516), mouse anti-dsRNA K1 1:500 (SCICONS K1), rabbit anti-pMLKL 1:1,000 (CST 37333), rabbit anti-total MLKL (tMLKL) 1:1,000 (Abcepta AP14272b), rabbit anti-pRIPK3 1:1,000 (CST 91702), rabbit anti-total RIPK3 (tRIPK3) 1:1,000 (ProSci Incorporated 2283), rabbit anti-pRIPK1 1:1,000 (CST 31122), rabbit anti-total RIPK1 (tRIPK1) 1:1,000 (CST 3493), mouse anti-ZBP1 1:1,000 (AdipoGen AG-20B-0010), rabbit anti-cleaved caspase-3 1:1,000 (CST 9661), rabbit anti-cleaved caspase-8 1:1,000 (CST 8592), and rabbit anti-gasdermin-D 1:1,000 (Abcam ab209845). For western blotting, HRP-conjugated donkey antirabbit was purchased from Jackson ImmunoResearch and HRP-conjugated goat anti-mouse was from Southern Biotech. Both were used at a dilution of 1:5,000. For immunofluorescence, donkey anti-mouse Alexa Fluor 488 and donkey anti-rabbit Alexa Fluor 594 were purchased from Jackson ImmunoResearch. Both were used at a dilution of 1:1,000. For nuclear staining, Hoechst nucleic acid stain (Thermo Fisher Scientific) was used at 1:1,000. To measure the levels of mouse IFN α , we used a mouse IFN alpha ELISA kit (ThermoFisher Scientific BMS6027). The pan-caspase inhibitor Z-VAD-FMK was purchased from MedChemExpress. The RIPK1 inhibitor GSK'963 was purchased from Sigma-Aldrich.

nsp15 Protein Purification. The codon-optimized MHV nsp15 sequence (GenScript) was cloned into a pET46 bacterial expression vector with a $10 \times$ N-terminal histidine tag. Site-directed mutagenesis (Agilent Technologies) was used to introduce mutations within nsp15. Constructs were transformed in C41 Escherichia coli cells. Cells were lysed and Ni-NTA agarose (Qiagen) was used to purify protein. Proteins were concentrated and subjected to size-exclusion chromatography. Additional details are provided in *SI Appendix*.

In Vitro nsp15 Cleavage Assay. Purified proteins (25 nM) were incubated with a 10-fold excess of a single-stranded 16-nucleotide RNA substrate (IDT) containing a 5' fluorescent tag and a single uridine cleavage site (6-FAM-GAAGCGAAACCCUAAG) for 2 h at 33 °C. The reaction contained 1× cleavage assay buffer (10 mM bis-tris, 10 mM sodium acetate pH 7, 1 mM DTT, and 5 mM MnCl₂). Reactions were stopped using an RNA loading buffer containing 95% formamide, 2 mM ethylenediaminetetraacetic acid (EDTA), and 0.1% (w/v) xylene cyanol. Reactions were run on 8 M urea 15% PAGE for 1 h at 220 V and imaged with a Typhoon FLA 9000 (Cytiva).

MHV Viral Infections. For infection, cells were plated and incubated overnight to obtain a confluent monolayer. The next day, cells were washed once with PBS and incubated with virus diluted in incomplete media for 1 h at 37 °C. Viral inoculum was removed and replaced with complete media or media containing 2% FBS.

MHV Replication Kinetics. WT or ifnar^{-/-} BMDMs were infected at an MOI of 0.2. At indicated times, supernatants were collected, spun down, and frozen at -80 °C. Viral titers were quantified by plaque assay performed using 17Cl-1 cells.

SARS-CoV-2 Infection of iAT2s and Vero E6 Cells. To measure viral replication kinetics in Vero E6 cells, cells were infected with WT virus or the E3A mutant at an MOI of 0.1. iAT2s were infected at an MOI of 0.3 for viral replication kinetics and ISG induction. Additional details are provided in SI Appendix.

Western Blot. BMDM cells were infected at an MOI of 1.0 for the indicated time. For evaluation of necroptosis, cells were treated with 20 μ M Z-VAD-FMK at 5 hpi. For evaluation of RIPK1-dependent necroptosis, cells were treated with 20 μ M Z-VAD-FMK and 100 nM GSK'963 at 5 hpi. Cells were washed and harvested in 1× PBS and then lysed with radio-immunoprecipitation assay buffer. Clarified lysates were subjected to western blot analysis. Additional details are provided in SI Appendix.

Coimmunoprecipitation of Coronavirus Replicase Proteins. BHK-R cells were plated in 10 cm dishes and incubated overnight. Cells were infected at an MOI of 0.01. At 16 hpi, cells were washed with $1 \times PBS$ and lysed in co-IP lysis buffer (0.5% NP-40, 50 mM Tris pH 8, 150 mM NaCl, and 5% glycerol) for 1 h at 4 °C. Protein G beads were bound to anti-nsp8 antibody according to the manufacturer's instructions (Thermo Fisher Scientific). Cleared lysates were incubated with antibody-bound beads overnight at 4 °C. Beads were washed with 1 × PBS containing 0.02% Tween-20 and eluted in 2× sample buffer. Input and co-IP samples were probed with anti-HA and anti-nsp8 antibodies by western blot.

Immunofluorescence Microscopy. For colocalization studies, 17Cl-1 cells were plated onto coverslips inserted into 24-well plates and incubated overnight. Cells were infected at an MOI of 1.0. At 6 hpi, cells were fixed with 3.7% formaldehyde and permeabilized with 0.1% Triton X-100. Samples were blocked with 5% normal donkey serum for 2 h. Primary antibody incubation was performed for 3 h with the following antibodies: anti-HA (1:1,000), anti-nsp8 (1:10,000), and Hoechst staining. Secondary antibody incubation was performed for 1 h and coverslips were mounted onto slides with Fluoro-Gel mounting medium (Fisher Scientific). Slides were imaged with a Deltavision Widefield Deconvolution microscope (GE) and images were processed using Imaris (Bitplane). For anti-dsRNA immunofluorescence, ifnar^{-/-} BMDMs were plated as mentioned above and infected at an MOI of 0.1. At 5 hpi, cells were fixed and permeabilized as described above. Samples were blocked with 5% normal donkey serum overnight. Primary antibody incubation was performed for 3 h with anti-dsRNA K1 (1:500) and Hoechst staining. Secondary antibody incubation was performed for 1 h and coverslips were mounted onto slides with Fluoro-Gel mounting medium (Fisher Scientific). Slides were imaged with a Deltavision Widefield Deconvolution microscope (GE) and images were processed using Imaris (Bitplane). The number of dsRNA puncta per cell was quantified using Imaris.

RNA Isolation and qPCR. BMDM or AML12 cells were lysed with 350 μ L of RLT lysis buffer (Qiagen) per well. Total RNA was isolated with the RNeasy Mini Kit (Qiagen). cDNA was synthesized from 500 ng of RNA using the RT² First Strand Kit (Qiagen). qPCR was performed using the RT² SYBR Green qPCR Mastermix. Fold change was calculated using the $2^{-\Delta\Delta Ct}$ method. For ISG analysis of iAT2s, cells were harvested in TRI Reagent, and RNA was isolated according to the

manufacturer's instructions. cDNA was synthesized from 500 ng of RNA using the RT² First Strand Kit (Qiagen). qPCR was performed using the SsoAdvanced Universal Probes Supermix (Bio-Rad). All qPCR runs were performed on a Bio-Rad CFX Opus 96 Real-Time PCR system. Additional details are provided in *SI Appendix*.

RNA Degradation. RNA degradation patterns of WT MHV-A59 and nsp15 mutant-infected RNA were measured using an Agilent 2100 Bioanalyzer system. Briefly, 1 microliter of extracted RNA was measured using the Eukaryote Total RNA assay following the standard protocol of the RNA 6000 Nano Kit (Agilent).

Mouse Infections. All mouse experiments were performed according to protocols approved by the Loyola University Chicago Institutional Animal Care and Use Committee. C57BL/6 male mice were intraperitoneally inoculated with 6×10^4 PFU of either WT-A59, H262A, L2D, or E3K. For infection of *ifnar*^{-/-} mice, mice were inoculated with 50 PFU of either WT-A59, H262A, L2D, or E3K. Additional details are provided in *SI Appendix*.

Histology. Formalin-fixed liver samples were submitted to the Loyola Department of Pathology and Laboratory Medicine for sectioning and hematoxylin and eosin staining. Slides were imaged with an Olympus BX46 microscope and 10 × objective. Images were evaluated for the number of necroinflammatory foci per field.

RNA Sequencing. Whole transcriptome sequencing was performed at the University of Chicago Genomics Facility. Raw read quality was examined using FastQC (http://www.bioinformatics.babraham.ac.uk/projects/fastqc/). Additional details are provided in SI Appendix.

Cell Viability. WT BMDMs were infected at an MOI of 0.1. At the indicated timepoint, cells were lysed with the CellTiter-Glo 2.0 cell viability assay (Promega) according to the manufacturer's instructions. Luminescence was measured using a GloMax Discover microplate reader (Promega).

Quantification and Statistical Analysis. Unpaired t tests and ANOVA tests were performed using GraphPad Prism 10. Statistical details can be found in the figure legends. Data are represented as mean \pm SD, as indicated in the figure legends. The nsp15 NTD protein sequence alignment was performed using SnapGene 7.0.1.

Data, Materials, and Software Availability. The RNA sequencing data of the WT MHV-A59 and nsp15 mutant-infected BMDMs have been deposited in the Sequence Read Archive under the BioProject accession number PRJNA1130930 (63) Protein sequences used in the nsp15 NTD alignment were analyzed from the following GenBank accession numbers: NC_048217.1 (MHV-A59), ON554096.1 (OC43), MT121215.1 (SARS-CoV-2), NC_004718.3 (SARS-CoV), OP712625.1 (MERS-CoV), KJ184549.1 (PEDV), KF514433.1 (229E), ON554022.1 (NL63), ON128612.1 (HKU1), KF430219.1 (Bat coronavirus CDPHE15), and MT239440.1 (FIPV) (64–74). All other data are included in the manuscript and/or SI Appendix.

ACKNOWLEDGMENTS. We thank Summer Jordan for maintaining Zbp1^{-/-} mouse lines and harvesting samples. We thank Dr. Michaela U. Gack for providing the CPER linker plasmid. We also thank Baker lab colleagues Dr. Amornrat O'Brien and Dr. Mudassir Ali for their support and suggestions on this manuscript. We thank Dr. Peter Larsen from the Loyola Genomics Core Facility for use of the bioanalyzer. This work was supported by NIH R01 Al159945 (to R.N.K., M.S., and S.C.B.) and R01 HL095993 and N01 75N92020C00005 (to D.N.K.). M.E. received support from NIHT32 Al007508, and F.R.M. was supported by a Diversity Supplement to R01 AI159945.

Author affiliations: ^aDepartment of Microbiology and Immunology, Stritch School of Medicine, Loyola University Chicago, Maywood, IL 60153; ^bDepartment of Biochemistry and Cell Biology, Boston University Chobanian and Avedisian School of Medicine, Boston University, Boston, MA 02118; ^cNational Emerging Infectious Diseases Laboratories, Boston University, Boston, MA 02118; ^dCenter for Regenerative Medicine, Boston University and Boston Medical Center, Boston, MA 02118; ^eThe Pulmonary Center and Department of Medicine, Boston University Chobanian and Avedisian School of Medicine, Boston, MA 02118; Department of Biochemistry, College of Agricultural and Life Sciences, University of Wisconsin-Madison, Madison, WI 53706; gDepartment of Molecular, Cell, and Developmental Biology, University of California, Santa Cruz, CA 95064; and ^hDepartment of Pathology, Delnor Hospital-Northwestern Medicine, Geneva, IL 60134

- J. M. Minkoff, B. tenOever, Innate immune evasion strategies of SARS-CoV-2. Nat. Rev. Microbiol. 21, 178-194 (2023).
- R. Gosert, A. Kanjanahaluethai, D. Egger, K. Bienz, S. C. Baker, RNA replication of mouse hepatitis virus takes place at double-membrane vesicles. J. Virol. 76, 3697-3708 (2002).
- K. Knoops et al., SARS-coronavirus replication is supported by a reticulovesicular network of modified endoplasmic reticulum. PLoS Biol. 6, 1957-1974 (2008).
- G. Wolff et al., A molecular pore spans the double membrane of the coronavirus replication organelle. Science 369, 1395-1398 (2020).
- X. Deng et al., Coronavirus nonstructural protein 15 mediates evasion of dsRNA sensors and limits apoptosis in macrophages. *Proc. Natl. Acad. Sci. U.S.A.* **114**, E4251–E4260 (2017).
- E. Kindler et al., Early endonuclease-mediated evasion of RNA sensing ensures efficient coronavirus replication. PLoS Pathog. 13, e1006195 (2017).
- C. E. Comar et al., MERS-CoV endoribonuclease and accessory proteins jointly evade host innate immunity during infection of lung and nasal epithelial cells. Proc. Natl. Acad. Sci. U.S.A. 119,
- e2123208119 (2022). C. J. Otter et al., SARS-CoV-2 nsp15 endoribonuclease antagonizes dsRNA-induced antiviral signaling. Proc. Natl. Acad. Sci. U.S.A. 121, e2320194121 (2024).
- R. Karki et al., ZBP1-dependent inflammatory cell death, PANoptosis, and cytokine storm disrupt IFN therapeutic efficacy during coronavirus infection. Sci. Immunol. 7, eabo6294 (2022)
- K. Liang et al., Initiator cell death event induced by SARS-CoV-2 in the human airway epithelium. Sci. Immunol. 9, eadn0178 (2024).
- S. Li et al., SARS-CoV-2 Z-RNA activates the ZBP1-RIPK3 pathway to promote virus-induced inflammatory responses. Cell Res. 33, 201-214 (2023).
- 12. K. A. Ivanov et al., Major genetic marker of nidoviruses encodes a replicative endoribonuclease. Proc. Natl. Acad. Sci. U.S.A. 101, 12694-12699 (2004).
- K. Bhardwaj, L. Guarino, C. C. Kao, The severe acute respiratory syndrome coronavirus Nsp15 protein is an endoribonuclease that prefers manganese as a cofactor. J. Virol. 78, 12218-12224 (2004).
- E. J. Snijder et al., Unique and conserved features of genome and proteome of SARS-coronavirus, an early split-off from the coronavirus group 2 lineage. J. Mol. Biol. 331, 991-1004 (2003).
- 15 X. Deng, S. C. Baker, An "Old" protein with a new story: Coronavirus endoribonuclease is important for evading host antiviral defenses. Virology 517, 157-163 (2018).
- S. T. Shi et al., Colocalization and membrane association of murine hepatitis virus gene 1 products and de novo-synthesized viral RNA in infected cells. J. Virol. 73, 5957-5969 (1999).
- J. Athmer et al., In situ tagged nsp15 reveals interactions with coronavirus replication/transcription complex associated proteins. mBio 8, e02320-16 (2017).
- H. Kang et al., Biochemical and genetic analyses of murine hepatitis virus Nsp15 endoribonuclease. J. Virol. 81, 13587-13597 (2007).
- 19. M. Hackbart, X. Deng, S. C. Baker, Coronavirus endoribonuclease targets viral polyuridine sequences to evade activating host sensors. Proc. Natl. Acad. Sci. U.S.A. 117, 8094-8103 (2020).
- R. Choi et al., High-throughput screening of the ReFRAME, Pandemic Box, and COVID Box drug repurposing libraries against SARS-CoV-2 nsp15 endoribonuclease to identify small-molecule inhibitors of viral activity. PLoS One 16, e0250019 (2021).
- 21 Y. Kim et al., Tipiracil binds to uridine site and inhibits Nsp15 endoribonuclease NendoU from SARS-CoV-2. Commun. Biol. 4, 193 (2021).
- M. Saramago et al., The nsp15 nuclease as a good target to combat SARS-CoV-2: Mechanism of 22 action and its inactivation with FDA-Approved drugs. Microorganisms 10, 342 (2022).
- J. Chen et al., Reversible and irreversible inhibitors of coronavirus Nsp15 endoribonuclease. J. Biol. Chem. 299, 105341 (2023).
- L. A. Guarino et al., Mutational analysis of the SARS virus Nsp15 endoribonuclease: Identification of residues affecting hexamer formation. J. Mol. Biol. 353, 1106-1117 (2005).
- K. Bhardwaj et al., Structural and functional analyses of the severe acute respiratory syndrome coronavirus endoribonuclease Nsp15. J. Biol. Chem. 283, 3655-3664 (2008).
- L. Zhang et al., Structural and biochemical characterization of endoribonuclease Nsp15 encoded by middle east respiratory syndrome coronavirus. J. Virol. 92, e00893-18 (2018).
- J. S. Joseph et al., Crystal structure of a monomeric form of severe acute respiratory syndrome 27. coronavirus endonuclease nsp15 suggests a role for hexamerization as an allosteric switch. J. Virol. 81, 6700-6708 (2007).
- 28 M. N. Frazier et al., Characterization of SARS2 Nsp15 nuclease activity reveals it's mad about U. Nucleic Acids Res. 49, 10136-10149 (2021).
- I. M. Wilson, M. N. Frazier, J. L. Li, T. A. Randall, R. E. Stanley, Biochemical characterization of 29 emerging SARS-CoV-2 Nsp15 endoribonuclease variants. J. Mol. Biol. 434, 167796 (2022).
- 30 S. Torii et al., Establishment of a reverse genetics system for SARS-CoV-2 using circular polymerase extension reaction. Cell Rep. 35, 109014 (2021).
- A. A. Amarilla et al., A versatile reverse genetics platform for SARS-CoV-2 and other positive-strand RNA viruses. Nat. Commun. 12, 3431 (2021).
- G. Q. Liu, M. U. Gack, An optimized circular polymerase extension reaction-based method for functional analysis of SARS-CoV-2. Virol. J. 20, 63 (2023).
- R. M. Hekman et al., Actionable cytopathogenic host responses of human alveolar type 2 cells to 33. SARS-CoV-2. Mol. Cell 80, 1104-1122 (2020).
- H. Jiao et al., Z-nucleic-acid sensing triggers ZBP1-dependent necroptosis and inflammation. 34 Nature 580, 391-395 (2020).
- 35 S. Balachandran, E. S. Mocarski, Viral Z-RNA triggers ZBP1-dependent cell death. Curr. Opin. Virol. 51. 134-140 (2021).
- T. Zhang et al., Influenza virus Z-RNAs induce ZBP1-mediated necroptosis. Cell 180, 1115-1129 36 (2020)
- H. Koehler et al., Vaccinia virus E3 prevents sensing of Z-RNA to block ZBP1-dependent necroptosis. 37 Cell Host Microbe 29, 1266-1276 (2021).
- H. I. Muendlein et al., ZBP1 promotes LPS-induced cell death and IL-1β release via RHIM-mediated interactions with RIPK1. Nat. Commun. 12, 86 (2021).
- H. Koehler, D. Titus, C. Lawson, Cell-type dependence of necroptosis pathways triggered by viral infection. FEBS J. 291, 2388-2404 (2024).

- 40. R. A. Aglietti et al., GsdmD p30 elicited by caspase-11 during pyroptosis forms pores in membranes. Proc. Natl. Acad. Sci. U.S.A. 113, 7858-7863 (2016).
- J. Ding et al., Pore-forming activity and structural autoinhibition of the gasdermin family. Nature **535**, 111-116 (2016).
- C. Y. Taabazuing, M. C. Okondo, D. A. Bachovchin, Pyroptosis and apoptosis pathways engage in bidirectional crosstalk in monocytes and macrophages. Cell Chem. Biol. 24, 507-514.e4 (2017).
- Y. Wang et al., Cutting edge: Caspase-8 is a linchpin in caspase-3 and gasdermin D activation to control cell death, cytokine release, and host defense during influenza A virus infection. J. Immunol. 207, 2411-2416 (2021).
- S. S. Wright *et al.*, A bacterial toxin co-opts caspase-3 to disable active gasdermin D and limit macrophage pyroptosis. *Cell Rep.* **43**, 114004 (2024).
- V. Krähling, D. A. Stein, M. Spiegel, F. Weber, E. Mühlberger, Severe acute respiratory syndrome coronavirus triggers apoptosis via protein kinase R but is resistant to its antiviral activity. J. Virol. 83, 2298-2309 (2009).
- $\hbox{C. Von Roretz, I. E. Gallouzi, Protein kinase RNA/FADD/caspase-8 pathway mediates the proapoptotic and the proapoptotic content of the pro$ activity of the RNA-binding protein human antigen R (HuR). J. Biol. Chem. 285, 16806-16813 (2010).
- R. H. Silverman, Viral encounters with 2',5'-oligoadenylate synthetase and RNase L during the interferon antiviral response. J. Virol. 81, 12720-12729 (2007).
- A. C. Ferreira et al., SARS-CoV-2 engages inflammasome and pyroptosis in human primary monocytes. Cell Death Discov. 7, 43 (2021).
- E. Sefik et al., Inflammasome activation in infected macrophages drives COVID-19 pathology. Nature 606, 585-593 (2022).
- X. Deng et al., Coronavirus endoribonuclease activity in porcine epidemic diarrhea virus suppresses type I and type III interferon responses. J. Virol. 93, e02000-18 (2019).
- B. A. Brown Ii, K. Lowenhaupt, C. M. Wilbert, E. B. Hanlon, A. Rich, The Z domain of the editing enzyme dsRNA adenosine deaminase binds left-handed Z-RNA as well as Z-DNA. Proc. Natl. Acad. Sci. U.S.A. 97, 13532-13536 (2000).
- D. Placido, B. A. Brown, K. Lowenhaupt, A. Rich, A. Athanasiadis, A left-handed RNA double helix bound by the $Z\alpha$ domain of the RNA-editing enzyme ADAR1. Structure 15, 395-404 (2007).
- T. A. Schweizer et al., Blunted sFasL signalling exacerbates TNF-driven neutrophil necroptosis in critically ill COVID-19 patients. Clin. Transl. Immunol. 10, e1357 (2021).
- G. Frühbeck et al., FNDC4 and FNDC5 reduce SARS-CoV-2 entry points and spike glycoprotein S1-induced pyroptosis, apoptosis, and necroptosis in human adipocytes. Cell Mol. Immunol. 18, 2457-2459 (2021).
- C. Steenblock et al., Viral infiltration of pancreatic islets in patients with COVID-19. Nat. Commun. 12, 3534 (2021).
- M. Koupenova et al., SARS-CoV-2 initiates programmed cell death in platelets. Circ. Res. 129, 631-646 (2021).
- Z. Huang et al., RIP1/RIP3 binding to HSV-1 ICP6 initiates necroptosis to restrict virus propagation in mice. Cell Host Microbe 17, 229-242 (2015).
- 58. A. Gautam et al., Necroptosis blockade prevents lung injury in severe influenza. Nature 628, 835-843 (2024).
- S. Balachandran, G. F. Rall, Benefits and perils of necroptosis in influenza virus infection. J. Virol. 94, e01101-19 (2020).
- R. Channappanavar et al., Dysregulated type I interferon and inflammatory monocyte-macrophage responses cause lethal pneumonia in SARS-CoV-infected mice. Cell Host Microbe 19, 181-193 (2016).
- K. D. Alysandratos et al., Patient-specific iPSCs carrying an SFTPC mutation reveal the intrinsic alveolar epithelial dysfunction at the inception of interstitial lung disease. Cell Rep. 36, 109636 (2021).
- K. J. Ishii et al., TANK-binding kinase-1 delineates innate and adaptive immune responses to DNA vaccines. Nature 451, 725-729 (2008).
- S. Feng, M. Evdokimova, S.C. Baker, Transcriptomics of Mouse Hepatitis Virus Strain A59 and nsp15 NTD mutants infected C57bl/6 Bone Marrow Derived Macrophages. NIH NCBI BioProject SRA. https://www.ncbi.nlm.nih.gov/PRJNA1130930. Deposited 2 July 2024.
- 64. S. E. Coley et al., Data from "Murine hepatitis virus strain A59, complete genome." GenBank. https:// www.ncbi.nlm.nih.gov/nuccore/NC 048217.1. Accessed 20 September 2024.
- W.-C. Cao et al., Data from "Human coronavirus OC43 isolate HCoV-OC43/BIME422-80/2019, complete genome." GenBank. https://www.ncbi.nlm.nih.gov/nuccore/ON554096.1. Accessed 20 September 2024.
- R. Zhang et al., Data from "Severe acute respiratory syndrome coronavirus 2 isolate SARS-CoV-2/ human/CHN/SH01/2020, complete genome." GenBank. https://www.ncbi.nlm.nih.gov/nuccore/ MT121215.1. Accessed 20 September 2024.
- R. He et al., Data from "SARS coronavirus Tor2, complete genome." GenBank. https://www.ncbi.nlm. nih.gov/nuccore/NC_004718.3. Accessed 20 September 2024.
- A. Kandeil et al., Data from "Middle East respiratory syndrome-related coronavirus isolate MERS-CoV/dromedary camel/Egypt/NC4714/2016, complete genome." GenBank. https://www.ncbi.nlm. nih.gov/nuccore/OP712625.1. Accessed 20 September 2024.
- 69. E. Poulsen, Y. Li, J. Bai, Y. Fang, Data from "Porcine epidemic diarrhea virus strain USA/KS/2013, complete genome." GenBank. https://www.ncbi.nlm.nih.gov/nuccore/KJ184549.1. Accessed 20 September 2024.
- C. D. Town et al., Data from "Human coronavirus 229E strain 229E/human/USA/933-40/1993, complete genome." GenBank. https://www.ncbi.nlm.nih.gov/nuccore/KF514433.1. Accessed 20 September 2024
- W.-C. Cao et al., Data from "Human coronavirus NL63 isolate HCoV-NL63/BIME412-77/2019, complete genome." GenBank. https://www.ncbi.nlm.nih.gov/nuccore/ON554022.1. Accessed 20 September 2024
- X. Chen, Q. Li, Z. Xie, Data from "Human coronavirus HKU1 isolate WZ17244, complete genome." GenBank. https://www.ncbi.nlm.nih.gov/nuccore/ON128612.1. Accessed 20 September 2024.
- C. D. Town et al., Data from "Bat coronavirus CDPHE15/USA/2006, complete genome." GenBank. https://www.ncbi.nlm.nih.gov/nuccore/KF430219.1. Accessed 20 September 2024.
- X. Zheng, S. Lu, G. Zhu, Data from "Feline coronavirus strain ZJU1709, complete genome." GenBank. https://www.ncbi.nlm.nih.gov/nuccore/MT239440.1. Accessed 20 September 2024.